

Localized Tissue Surrogate Deformation due to Controlled Single Bubble Cavitation

Y. Hong¹ · M. Sarntinoranont¹ · G. Subhash¹ · S. Canchi¹ · M.A. King²

Received: 28 October 2014 / Accepted: 6 April 2015 / Published online: 18 April 2015
© Society for Experimental Mechanics 2015

Abstract Cavitation-induced shock wave, as might occur in the head during exposure to blast waves, was investigated as a possible damage mechanism for soft brain tissues. A novel experimental technique was developed to visualize and control single bubble cavitation and its collapse, and the influence of this process on a nearby tissue surrogate was investigated. The experiment utilized a Hopkinson pressure bar system which transmits a simulated blast pressure wave (with over-pressure and under-pressure components) to a fluid-filled test chamber implanted with a seed gas bubble. Growth and collapse of this bubble was recorded during passage of the blast wave with a high speed camera. To investigate the potential for cavitation damage to a tissue surrogate, local changes in strain were measured in hydrogel slices placed in various configurations next to the bubble. The strain measurements were made using digital image correlation (DIC) technique by monitoring the motion of material points on the tissue surrogate. In one configuration, bubble contact dynamics resulted in compression contact ($>60 \mu\text{s}$) followed by inertially-driven tension ($>140 \mu\text{s}$). In another configuration, the influence of local shock waves emanating from collapsed bubbles was captured. Large compressive strains (0.25 to 0.5) that were highly localized (0.18 mm^2) were measured over a short time period ($<24 \mu\text{s}$) after bubble collapse. High bubble collapse pressures 29 to 125 times that of peak blast overpressure are predicted to be the source of these

large strains. Consistent with theoretical predictions, these cavitation-based strains are far larger than the strains imposed by passage of the simulated blast wave alone. Finally, the value of this experimental platform to investigate the single bubble cavitation-induced damage in a biological tissue is illustrated with an example test on rat brain slices.

Keywords Cavitation collapse · Traumatic brain injury · Agarose hydrogel · Shock wave · Brain tissue

Introduction

Blast-induced traumatic brain injury (bTBI) has sometimes been referred to as the ‘signature injury’ of the Iraq and Afghanistan wars, with estimates of 10 to 20 % of returning military personnel having suffered from bTBI [1]. Patients often present a complex response to bTBI, and persistent symptoms can lead to long-term disabilities. One key concern is that pathogenesis of bTBI and initial mechanisms of injury are still unclear. Numerous possible mechanisms, including diffuse axonal injury due to rapid accelerating – decelerating forces, skull deformation with elastic flexure, multiple wave reflections, impedance mismatch between heterogeneous tissue types, and cavitation, have been proposed [2]. Brain injury mechanisms based on cavitation are rooted on the concept of shock loading [3] where blast waves consist of large overpressure (compressive) and smaller underpressure (tensile) components. Propagating blast waves traveling through air impinge on the head, leading to a portion of the wave being transmitted into cerebrospinal fluid (CSF) and brain tissue. Within the short time period of blast wave transmission, there is potential for cavitation bubbles to form, grow and collapse within fluid spaces inside the head. Cavitation occurs spontaneously when liquid of approximately constant temperature is

✉ G. Subhash
subhash@ufl.edu

¹ Department of Mechanical & Aerospace Engineering, University of Florida, Gainesville, FL 32611, USA

² Department of Pharmacology & Therapeutics, University of Florida, Gainesville, FL 32611, USA

subjected to a sufficiently rapid decrease in pressure. Vapor bubbles form when pressure falls below the saturated vapor pressure as may occur during the passage of underpressure phase of a blast wave. CSF carries dissolved gasses, and cavitation can be induced within CSF or other fluid compartments within the brain when exposed to relatively low blast underpressure [4]. Nucleation of cavitation bubbles may occur through heterogeneous nucleation, initiating at junctions of liquid–solid boundaries, e.g., particulate surfaces. However, pre-existing gas nuclei can act as another source [5]. Previous hyperbaric decompression and ultrasound studies suggest that bubbles originate from microscopic gas nuclei present in biological tissues [6–9].

Spatial displacement associated with formation and growth of vapor bubbles with cavitation could be sufficient to damage brain tissue. Furthermore, considerable energy is released with bubble collapse, and this generates additional local shock waves that can be of very high frequency and magnitude [10, 11]. Bubble collapse pressures, which drive these local shock waves, have been reported over a wide range (15 MPa to 2.5 GPa) [11–14]. These pressures are potentially much greater than blast overpressures. Another characteristic feature of bubble collapse is the generation of a high-speed fluid jet [15, 16] which may cause additional damage as it impinges on tissue. Resulting collapse events can mediate highly localized tissue deformation and damage. Such cavitation damage of material surfaces is well established since the original work of Rayleigh who first studied pitting of ship propeller blades or water turbine blades [17, 18], which is commonly referred to as ‘cavitation erosion’. Thus, collapsing cavitation bubbles in the brain may cause local damage to nearby tissues or blood vessels.

While limitations of current imaging techniques make *in vivo* cavitation measurements challenging, previous studies suggest that extensive cavitation caused by explosive blast might occur in the CSF surrounding human brain [19, 20]. For example, negative pressures have been reported in CSF following exposure to blast waves generated by shock tubes in cadaver and animal models [21]. Other studies using simplified fluid models of the head or head-neck have also shown negative pressure to be induced at the contrecoup position when exposed to a high pressure blast wave directed at coup [3, 22, 23]. *In vitro* impact and blast studies also show visual evidence of cavitation [3, 24]. TBI impact studies using transparent, fluid-filled head models showed visual evidence of bubble formation, growth and collapse within CSF spaces [23]. In shock tube blast tests, Goeller et al. [3] also showed cavitation at contrecoup regions that coincided temporally with periods of negative pressure. Collapse of cavitation bubbles and elastic rebound of the skull resulted in significant pressure spikes in CSF fluid regions. Other computational studies of blast propagation through the head and surrounding CSF spaces predict regions of negative pressure in contrecoup regions which also suggest cavitation may occur during blasts

[13, 14, 19, 20, 25]. Tissue studies using ultrasound shock waves also support cavitation induced damage, e.g., hemorrhage and cellular membrane poration due to lithotripsy [26, 27], though these studies occur at a different frequency range than blasts. In addition, cavitation in blood vessels has been shown to result in air emboli that can reach the brain causing cerebral infarct [28, 29].

There are numerous studies of bubble dynamics during cavitation. The most common theoretical model is the Rayleigh-Plesset model [17, 18]. Plesset and Chapman were the first to calculate liquid jet formation with collapse of an empty spherical bubble due to the high surrounding fluid pressure [18]. Experimental evidence of cavitation is often given by acoustic measurements [30] and/or optical imaging [11]. Pressure amplitudes during cavitation bubble collapse have been experimentally determined to be between 15 MPa [14] to 1 GPa [12] using pressure measurement systems. By using Rayleigh-Plesset theory with bubble imaging data, maximum collapse pressures over a wide range between 8 MPa [13] to 2.5 GPa [11] have also been calculated.

A fundamental problem in the study of cavitation is that a testing platform does not readily exist to control bubble growth and collapse. In this study, a novel experimental system capable of investigating single bubble cavitation under conditions relevant to blast was developed. This experiment utilized a polymer Hopkinson pressure bar system to transmit a simulated blast pressure wave to a fluid-filled test chamber [31]. By controlling the gas content in the fluid chamber, either bulk or single bubble cavitation tests can be performed. For single bubble tests, controlled cavitation was produced by introducing a seed gas bubble which underwent growth and collapse with blast wave passage. Cavitation was then investigated as a possible damage mechanism for soft tissues such as brain by quantifying the dynamic behavior of a nearby tissue surrogate (ballistic gel or 0.5 % agarose hydrogel). Deformation of speckled hydrogel slices were recorded with a high speed camera, and a digital image correlation (DIC) technique was used to calculate strain fields during bubble growth and collapse. The subsequent response of the tissue surrogate to the local blast wave resulting from single bubble collapse was captured and quantified. Implications for localized high strain due to bubble collapse are discussed. Such a test system may be used to better isolate damage and injury due to cavitation bubbles and, in future studies, this system will be extended to biological tissues such as brain tissue slices.

Experimental Method

High Strain Rate Test System

A split Hopkinson pressure bar (SHPB) is traditionally used to test metallic and ceramic materials at high strain rates in the

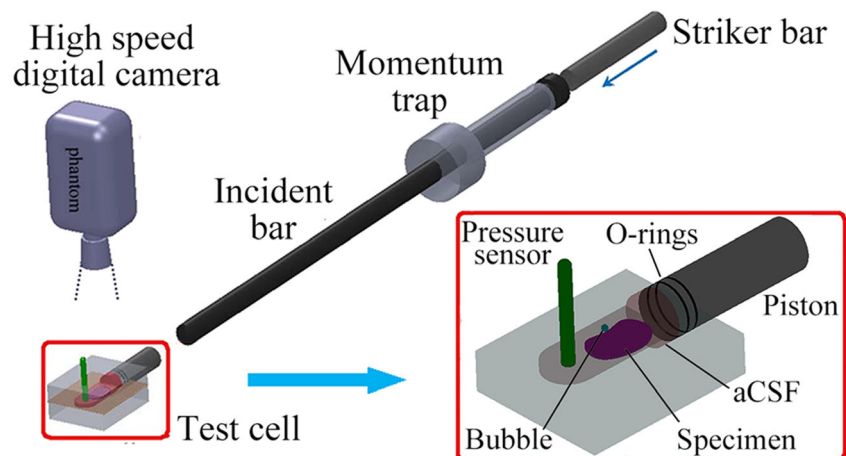
range of 500–5000/s [32, 33]. In this study, a polymer SHPB (PSHPB) system [31, 34–36] was used to generate lower magnitude stress and pressure waves in a fluid-filled acrylic test cell that mimicked shock waves generated within the head. A schematic of the test system is given in Fig. 1. The striker bar (0.0254 m diameter and 0.38 m in length) was launched from a gas gun towards the incident bar (0.0254 m diameter and 2.44 m in length). This impact sends a stress wave through the incident bar, and upon reaching the piston, the stress wave accelerates the piston rapidly causing a stress wave to be generated in the fluid. After the initial compression, a momentum trap pulls back the incident bar in order to avoid multiple loading of the test cell [33] which also retracts the piston due to the stiff O-ring that seals the fluid. This process releases the pressure on the fluid in the test chamber and generates a tensile tail in the pressure profile. Thus, both the over-pressure and under-pressure components are generated, similar to a blast wave profile.

The 90×55×42 mm transparent acrylic test cell consisted of an interior rectangular chamber filled with 6 ml of distilled water to house the fluid and gel slices. The interior chamber was connected to a cylindrical chamber in which the piston was fit. The cylindrical chamber was machined for a tight fit with the piston rod, also O-rings mounted on the piston provided a leak-proof seal. The gauge pressure inside the chamber during the testing process was measured utilizing a high rate pressure sensor (113B24, PCB Piezotronics Inc., Depew, New York) with a sample rate of 2 MHz. In addition, a high speed digital camera (Vision Research 710, Ametek Company, Wayne, New Jersey) was aligned above the test cell to view cavitation events at a rate of 80,000 to 200,000 frames/second.

Cavitation Testing

For bulk cavitation testing, specimen samples were submerged in the test cell and tested with the PSHPB system.

Fig. 1 Schematic of the momentum-trap PSHPB experimental set-up used for cavitation testing of tissue surrogates. The seed bubble and hydrogel slice specimen were placed in the fluid filled test cell and loaded by the incident bar of PSHPB. The striker bar was launched by a gas gun



No bubbles were visible in the test cell before testing. For single bubble cavitation tests, the fluid-filled test chamber was degassed to prevent the formation of multiple bubbles. To accomplish this, all parts of the test chamber were submerged in distilled water in a large beaker and degassed within a vacuum pump (model 150, Precision scientific Inc., Winchester, Virginia) for 10 min. An ultrasonic bath (model FS20, Fisher Scientific Inc., Hampton, New Hampshire) was then used to release and remove remaining small bubbles from all surfaces. A single seed bubble with a diameter of less than 50 μm was picked up with a spatula from outside the chamber and then placed along an inside wall of the submerged test cell. To ensure proper placement, either a small piece of tape was adhered to the chamber wall or a small region of the chamber wall was coated with petroleum (model p-16, Panef Co., Milwaukee, Wisconsin) to act as a surface anchor for the seed bubble, see Fig. 2.

Gel Slice Testing

Gel slices were introduced into the test cell to determine the effect of cavitation on soft tissue response. While initial tests were conducted using ballistic gel (10 %, product 1347, VYSE, Addison, IL), the majority of tests were conducted with agarose-based hydrogel (0.4–0.6 %, Trevigel 5000 powder, Trevigen, Inc. Gaithersburg, Maryland). Hydrogels were prepared in a Petri dish and cut into approximately 11×9×1 mm slices. Agarose-based hydrogels have been previously used for brain surrogate studies [37, 38]. Modulus values for this concentration (−0.27 kPa) are slightly higher than those measured for brain tissue slices [34, 37]. To allow tracking of deformation, hydrogel slices were speckled with black ink (Accu stamp, Cosco Industries Inc., Harwood Heights, Illinois) with an air brush (model 200nh, Badger Air-Brush Co., Franklin Park, Illinois). Once speckled on the hydrogel surface and allowed to dry in air, the ink remained stable when submerged for several days without evidence of diffusion.

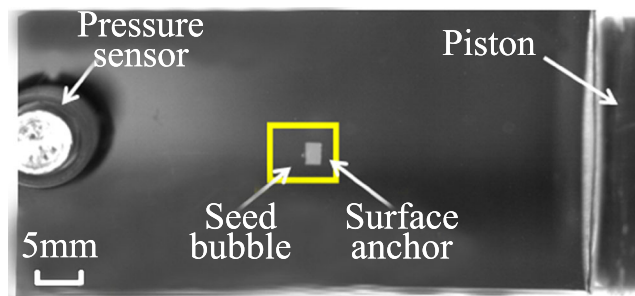


Fig. 2 Schematic of the degassed test chamber with a single seed bubble (top view as seen by the high speed camera)

Two bubble placements were tested: (i) at the edge and (ii) underneath slices. In both cases, hydrogel slices were placed without any anchoring to the test chamber wall. With edge placement (i), the seed bubble was placed near the edge of a hydrogel slice at a distance of approximately 1 mm within the plane of the hydrogel slice. This allowed for quantification of edge deformation during bubble growth and collapse. In the other test configuration (ii), the seed bubble was placed beneath the hydrogel close to the center of the slice. This placement resulted in better visualization of the local shock wave response of the tissue due to bubble growth and collapse.

Digital Image Correlation (DIC)

Digital image correlation is a well-established experimental technique to measure full-field displacements on any test sample which has been speckled with dye or ink. These speckles move with the object upon loading and by capturing the time resolved images of the deformed specimen, allow measurement of the displacement on the entire specimen. This technique has been employed by Subhash et al. [34] to measure tensile deformation of agarose gel at various concentrations as well as our previous brain slice testing [31]. In the current study, high speed camera images of the deforming hydrogels were used to calculate displacement and strain of the hydrogel slices using the DIC method. 2D-DIC was used to track the movement of material points between consecutive images. Reference undeformed hydrogel slice images were divided into an evenly spaced grid of dimension $(0.05 \times 0.05 \text{ mm})$ corresponding to the pixel size in each image. Each pixel had a different gray value intensity due to speckling. A sum of squared differences correlation criterion, zero-normalized sum of square differences (ZNSSD) correlation criterion [39], was employed to track the displacement of each pixel. For this method, a 29×29 pixel subset centered about an object pixel was selected within the reference image, and its corresponding location in the deformed image at the next time point was determined using the ZNSSD correlation function to evaluate the similarity between reference and target subsets. Newton–Raphson method with bicubic spline interpolation was employed to solve for the correlation function. Once the

minimum correlation value was determined, differences between the corresponding positions of reference and deformed subset centers yielded in-plane displacements. Strain fields were calculated from displacement fields using two-dimensional Savitzky-Golay digital differentiation [40]. The DIC algorithm was implemented using DIC software (MOIRE, v. 0.955b, Opticist.org) based on Pan et al. [40].

Estimation of Bubble Collapse Pressure

The Rayleigh-Plesset equation [18] was used to estimate bubble collapse pressure in order to quantify the local shock wave effect. The simplified model is based on an isolated spherical bubble cavitation in an infinite, incompressible liquid and does not account for surface tension or viscous effects. The dynamic bubble behavior is governed by the following differential equation [18]

$$R\ddot{R} + \frac{3}{2}\dot{R}^2 = \frac{P_R - P_\infty}{\rho} \quad (1)$$

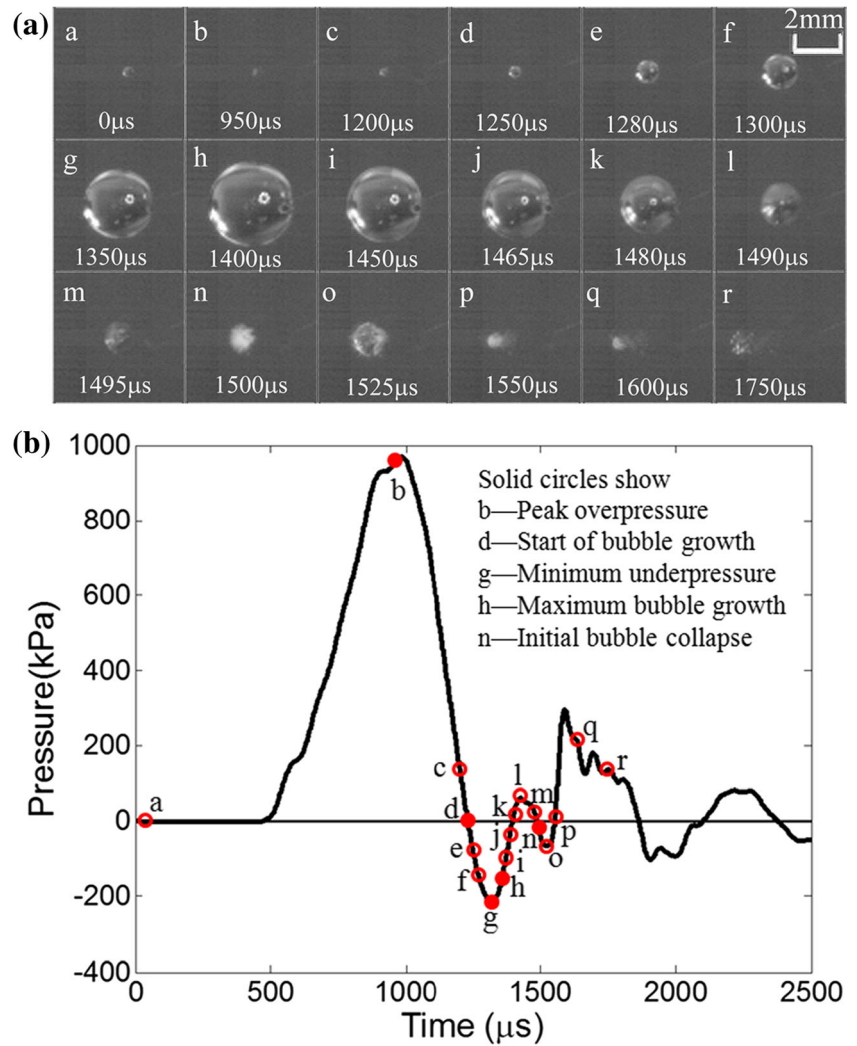
where R is the bubble radius, P_R is the pressure in the liquid at the boundary of the bubble, P_∞ is the environmental pressure, and ρ is the density of surrounding fluid. For each test, $R(t)$ was determined from high speed digital images. The central difference method was used to calculate time derivatives, and $P_\infty(t)$ was set as the far-field fluid pressure as measured by the pressure transducer. The time point of bubble collapse was also determined from imaging data as the point at which the bubble shrank to its smallest measurable radius.

Results

Single Bubble Cavitation

Figure 3(a) shows temporal evolution of a typical bubble with exposure to the simulated blast pressure wave shown in Fig. 3(b). The seed bubble was compressed during the compressive overpressure phase (a-c); the bubble grew during the tensile underpressure phase (d-h); the bubble collapsed (n); then there was secondary growth (o) followed by secondary collapse of the bubble (p-r). The bubble remained approximately spherical throughout the test until collapse. The time from when the bubble started to grow until collapse ranged from 270 to 350 μs . The corresponding pressure profile measured within the chamber was similar to a blast shock wave with an overpressure peak phase followed immediately by a negative pressure (underpressure) phase and subsequent smaller oscillations. Minimum bubble size occurred at approximately the time of maximum overpressure, $P_{o \text{ max}}$. Maximum bubble size was measured just after the minimum recorded underpressure, $P_{u \text{ min}}$. There was a time lag (50 to

Fig. 3 Dynamic behavior of a single bubble in response to a simulated blast wave. **a** Sequence of images showing evolution of a single bubble cavitation. The gas seed bubble had an initial diameter <math>< 50 \mu\text{m}</math>. **b** Corresponding pressure profile showing overpressure and underpressure phases. $t=0</math> corresponds to the start of the PSHPB experiment$



63 μs) between true minimum pressure and maximum bubble size. This delay was attributed to (i) the time required for the pressure wave to travel the distance between the bubble and sensor (30 mm) and (ii) inertial delay of bubble growth. Bubble collapse was noted at point (n) and corresponded to disintegration of the original bubble into multiple smaller bubbles.

Table 1 summarizes pressure and bubble behavior during PSHPB testing. For this test system, $P_{o\ max}$ ranged between 800 and 1200 kPa. $P_{u\ min}$ ranged between -50 and -250 kPa. The average ratio of overpressure to underpressure ($P_{o\ max} / |P_{u\ min}| = 5.12 \pm 0.45\text{SD}$) was relatively constant. Overall, increasing magnitude of air gun pressure increased the magnitude of $P_{u\ min}$ and resulted in increasing bubble size, see Fig. 4. As a result of this dependence, bubble behavior was grouped based on $P_{u\ min}$ into low, medium and high groups, see Table 1. Bubble collapse was consistently observed after the second overpressure peak (point l in Fig. 3, 85 ± 17 kPa) as pressure was falling. The measurable bubble collapse radius varied between 0.2 and 0.5 mm. It should be noted that bubble

radius at collapse was difficult to determine as the bubble size approached the limit of camera image resolution. Therefore, it was not possible to identify the pressure at the exact time of collapse of the bubble from the images. To overcome this limitation, we have plotted the instantaneous bubble radius R during its growth and collapse as shown in Fig. 5(a). A fifth-order polynomial was fit to this data from which one can calculate the corresponding and functions and then determine the boundary pressure P_R in the fluid for each bubble radius based on Rayleigh-Plesset relation as shown in Fig. 5(b). Because the radius at the instance of bubble collapse (i.e., at $R=0$) is unknown, we fit an exponential curve ($P_R = ke^{-R}$) for this data. The curve-fit equations for the growth and collapse of three typical bubble sizes are shown in Fig. 5(b). By setting $R=0$, we determined the elusive collapse pressure P_c at the time of bubble collapse i.e., $P_c = k$. Typical collapse pressure for a large size bubble (i.e., large negative or tensile pressures) were as high as 100 MPa. For comparison, note from Fig. 3(b) that a typical value of incident blast overpressure in our set up was only around 1 MPa, and the blast under pressure was

Table 1 Summary of test parameters and bubble behavior during single bubble cavitation tests

Underpressure group (sample size)	Low ($n=10$) –97 to –75 kPa	Medium ($n=8$) –205 to –127 kPa	High ($n=9$) –336 to –294 kPa
Average $P_{u\ min}$ (kPa)	-86 ± 11	-166 ± 39	-315 ± 21
Air gun pressure (kPa)	69	130	207
$P_{o\ max}$ (kPa)	851 ± 49	943 ± 71	1178 ± 22
Over/underpressure duration* (μs)	$586\pm 23/157\pm 14$	$643\pm 31/168\pm 22$	$723\pm 24/184\pm 13$
Lag time [†] (μs)	53 ± 2	58 ± 7	60 ± 3
Maximum radius of bubble (mm)	0.47 ± 0.12	1.08 ± 0.15	1.45 ± 0.11
Collapse radius (mm)	0.21 ± 0.11	0.24 ± 0.13	0.23 ± 0.09
P_{∞} at collapse [‡] (kPa)	6.51 ± 3.32	3.38 ± 7.44	0.51 ± 4.65
P_c (kPa)	$25.1\times 10^3\pm 4.2\times 10^3$	$68.6\times 10^3\pm 5.3\times 10^3$	$123.9\times 10^3\pm 10.2\times 10^3$
$P_c/P_{o\ max}$	–29.5	–72.7	–125.2

* Initial phases

† Between $P_{u\ min}$ and maximum bubble radius

‡ Chamber pressure measured away from the bubble

approximately 250 kPa. Thus the local pressure at the time of bubble collapse could be as high as 100 times the incident over pressure or approximately 400 times the blast under pressure. In our experiments, P_c was determined to be 29 to 125 times higher than the measured peak overpressure.

Hydrogel Deformation: High Pressure Cavitation Testing

Initial gel studies were conducted at high blast pressures using fluid chambers that were not degassed. PSHPB testing of

these test cells resulted in multiple bubble formation and cavitation within the test chamber. Figure 6 shows bubble initiation (b) and growth (c & d) near a gel edge in a degassed test chamber. These experiments showed clear evidence of shock wave generation with bubble collapse (f) that resulted in hydrogel indentation (g-i) well after the bubble has collapsed. Thus, this test showed proof of bubble collapse and local shock wave deformation at high pressure; other tests (next section) were conducted with more controlled bubble conditions and revealed the effect of cavitation at lower blast pressures.

Hydrogel Deformation: Single Bubble at an Edge

Single cavitation bubble tests in degassed chambers provided more consistent bubble placement –1 mm from the side edge of the hydrogel slice. Single bubble dynamics (growth and collapse) were similar to that described in the previous section conducted using a similar blast profile. Hydrogel deformation with direct bubble contact was captured with blast wave propagation, while the effect of local shock waves from bubble collapse was not detected. Measured strains in the vicinity of the bubble were much larger than those which occurred during passage of the compressive 1D overpressure wave through the hydrogel (<0.002, detectable strain limit). Figure 7 shows typical hydrogel deformation during bubble growth and collapse. As the bubble grew, the hydrogel edge was deformed by direct contact with the expanding bubble. Radial strain (ε_{rr}), circumferential strain ($\varepsilon_{\theta\theta}$) and von Mises strain (ε_{VM}) are shown in Fig. 7. It should be noted that deformation and strain fields were not calculated in regions where the bubble overlapped the edge of the hydrogel (masked regions) since there was distortion of the observed

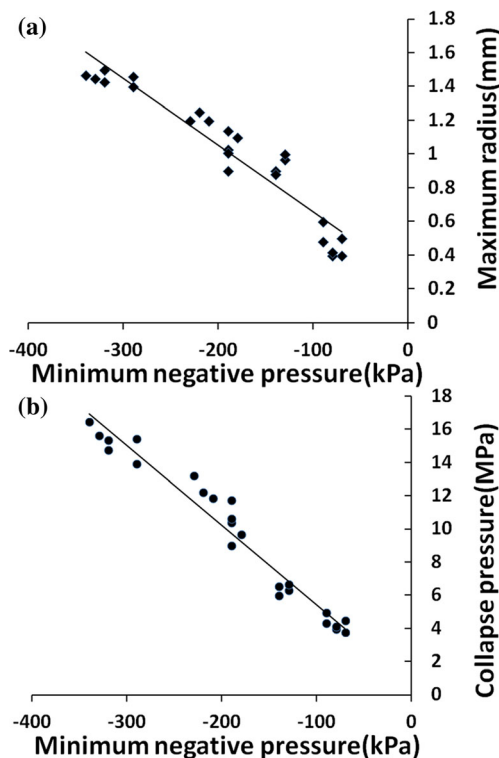


Fig. 4 Bubble radius variation with minimum underpressure, $P_{u\ min}$. A linear function was fit ($R^2=0.90$)

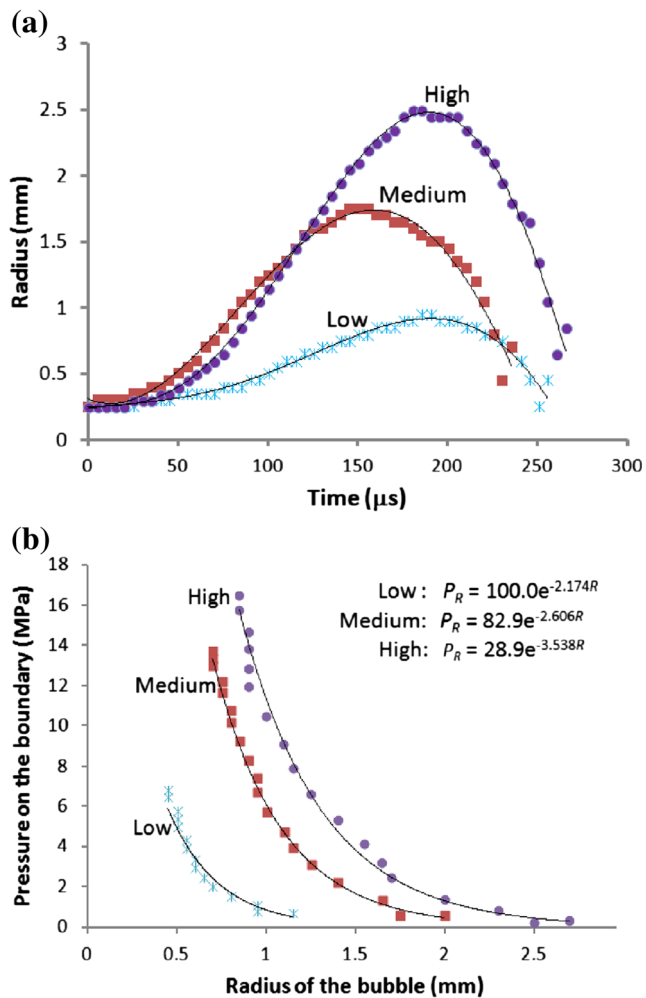


Fig. 5 Bubble time history and calculated collapse pressure. **a** Typical bubble growth and collapse during testing. Radial profiles for three bubbles corresponding to low, medium and high underpressure groups are shown. 5th order polynomials were fit to experimental data ($R^2 > 0.95$). **b** Collapse pressure estimation method. Bubble pressure was calculated at each bubble radius for the low, medium and high underpressure tests shown in (a). Exponential equations were fit and pressure at $r=0$ was estimated to be the bubble collapse pressure, P_c ($R^2 > 0.90$)

speckle field due to the overlapping bubble. As these regions experience maximum strain, the values close to the edge could not be calculated. Overall, large deformations were captured and magnitude of calculated strains decreased with distance from the bubble center.

To show dynamic behavior, radial strain of a material point along the edge and nearest to the bubble is shown in Fig. 8. ε_{rr} increased in magnitude and became more compressive during bubble growth, reaching a peak value (-0.15 ± 0.03 , see Table 2) when the bubble grew to maximum size ($1230 \pm 162 \mu\text{s}$). The collapse process of the bubble was much faster compared to the retraction time of the hydrogel due to the inertia associated with the higher density of hydrogel. As the bubble shrank, compressive ε_{rr} strains of the hydrogel

returned to zero. Due to inertial effects, the hydrogel edge continued to deform past its original position, resulting in tensile ε_{rr} . Another peak of inertially-driven tensile strain (0.12 ± 0.02) occurred $65 \pm 5 \mu\text{s}$ after the time point of maximum compression. Maximum calculated strain values are given in Table 2. For all tests, the maximum compressive ε_{rr} was slightly greater than the maximum tensile ε_{rr} , and the ratio of strain magnitudes for maximum inertial tensile strain to maximum compressive strain was 0.87 ± 0.05 .

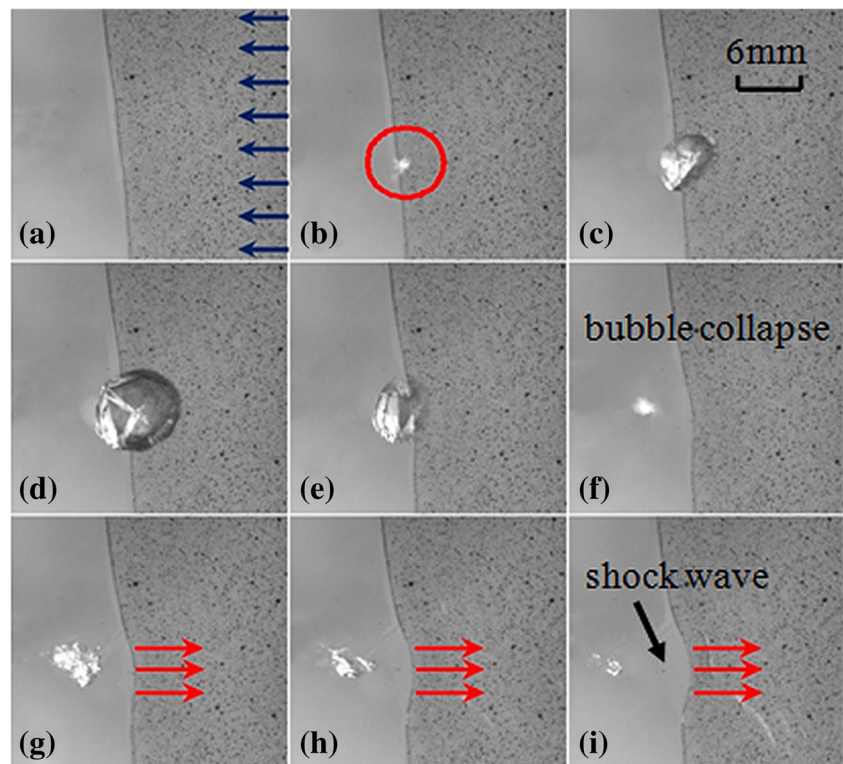
The effect of local shock wave generation following bubble collapse was not seen by changes in ε_{rr} for this bubble configuration (no compressive strains after bubble collapse). This was because either the edge of the hydrogel was not sufficiently close to the center of the bubble to sense the shock wave, or the expanding bubble pushed the entire hydrogel slice away from the bubble rather than inducing local deformation.

Hydrogel Deformation: Single Bubble Underneath a Tissue Slice

To better capture effects of the local shock wave generated with bubble collapse, a single seed bubble was placed underneath the hydrogel slice to provide more continuous contact with the tissue surrogate during the simulated blast. Figure 9 shows a series of high speed images for a typical experiment of bubble growth (b-c) and collapse (d-e) on the left side of each image, and the calculated strain field in the hydrogel at that moment on the right side of each image. Bubble growth was captured due to transparency of hydrogel. The von Mises strain field was determined to be radially symmetric, and a clear circumferential ring pattern evolved with time. The strain amplitude at the center of the bubble reached a peak value with maximum bubble expansion (at c) and then decreased as the bubble collapsed (e). After the bubble collapsed (f), the local strain again increased at the center of the hydrogel. These large compressive strains are attributed to a localized shock wave originating from the collapsed bubble and propagating through the hydrogel.

A summary of strain field data is given in Table 2. During bubble growth, radial strains at the bubble edge are compressive. Circumferential strains at the bubble edge are tensile. Following collapse, highly localized compressive deformation resulted in maximum strain values (ε_{VM} ranged from 0.21 to 0.51) over a short duration ($< 24 \mu\text{s}$) at the location of the bubble center. These strains are larger than those determined during maximum bubble expansion. These strains are also much greater than during passage of the compressive 1D overpressure wave only (below detectable strain limit). Comparing with the previous test bubble configuration (edge placement, Figs. 7 and 8), these localized shock strains are slightly larger but over a shorter time period.

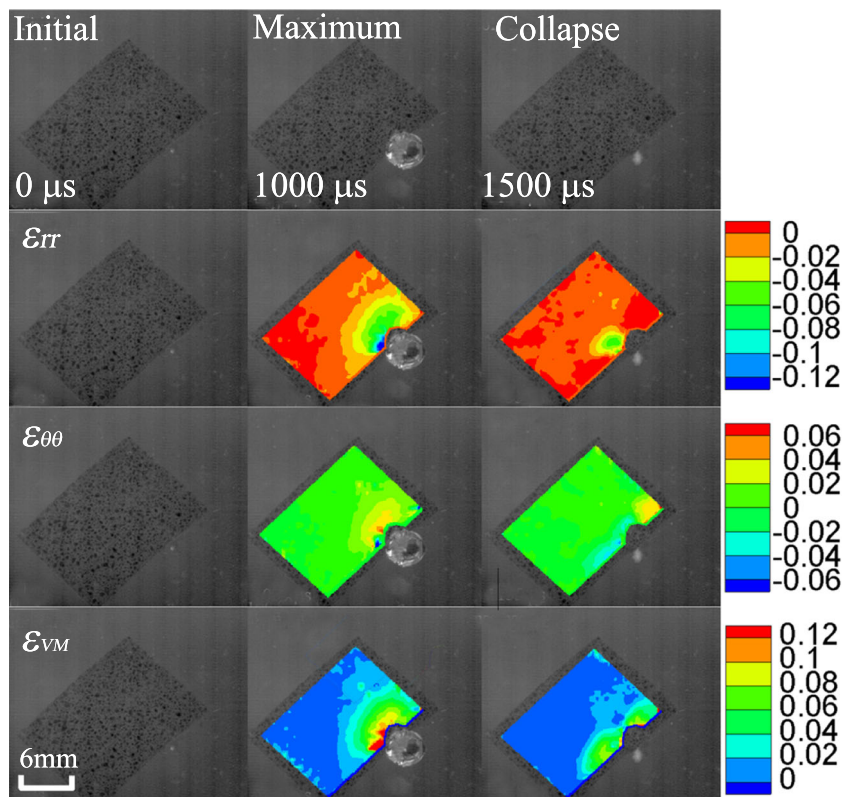
Fig. 6 Bulk cavitation and tracking of a single bubble near a ballistic gel edge. **a** shows the incident blast wave direction traveling from right to left (*blue arrows*), **b** bubble initiation (*circled*), **c** and **d** growth, **f** collapse, and the effect on an adjacent gel slice (**f** to **i**). A local shock wave following bubble collapse resulted in highly localized hydrogel deformation (*red arrows*). $P_{o\ max}=2800$ kPa and $P_{u\ min}=-380$ kPa



For each test, the calculated bubble collapse pressure was plotted against the maximum measured strain after bubble collapse, see Fig. 10. The local shock wave emanating from the

collapsed bubble is driven by this bubble collapse pressure, and the corresponding maximum strain was shown to clearly increase with this pressure value.

Fig. 7 Single bubble cavitation at the edge of an agarose hydrogel slice. (*Top row*) High speed images showing initial seed bubble at edge, maximum growth and collapse at selected times; (*2nd row*) radial strain, (*3rd row*) circumferential strain and (*4th row*) von Mises strain at the same time points. Regions at the edge were excluded due to masking by the impinging bubble. Test chamber was degassed before gas seed bubble (<50 μm diameter) was placed to the side of the hydrogel (-1 mm gap distance). $t=0$ corresponds to the start of the PSHPB experiment. Simulated blast wave traveled from right to left with $P_{o\ max}=1260$ kPa and $P_{u\ min}=-189$ kPa



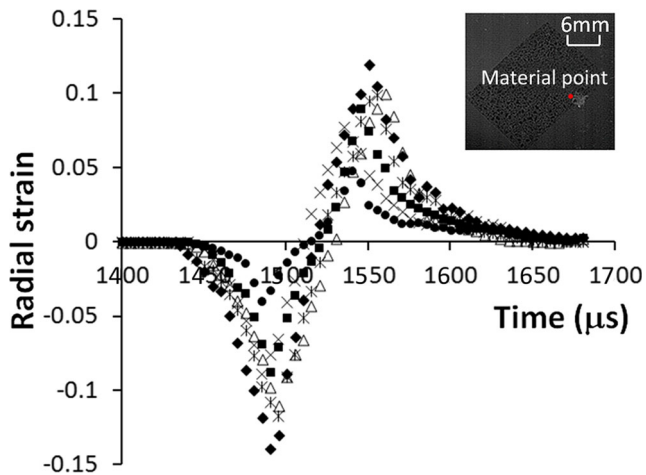


Fig. 8 Inertially-driven changes in radial strain in the hydrogel during bubble growth and collapse. The nearest hydrogel point to the seed bubble that was not covered by growing bubble was selected. The graph shows results for 6 different experiments. Gas seed bubbles (<50 μm diameter) were placed to the side of the agarose hydrogel (–1 mm gap distance). $t=0$ corresponds to the start of the PSHPB experiment

Discussion

In this study, we were able to visually capture single bubble growth and collapse as well as the effect of this single bubble cavitation on a nearby soft tissue surrogate. Overpressure and underpressure were controlled by gas gun pressure of a PSHPB system. By using this test system, we were able to approximately mimic the blast wave profile that would be transmitted to intracranial fluids. The high overpressure magnitudes and durations were within relevant ranges for blast injury [21, 41, 42] as measured *in vivo* in animal models

which allow for follow up assessment of injury to living tissue. Underpressure magnitudes were larger than those reported for blasts [1, 43] but within a relevant order of magnitude. We were able to capture major modes of potential cavitation bubble-tissue interaction including (i) compression contact of the bubble growth during the growth phase, (ii) tensile rebound during bubble collapse, and (iii) compressive strains generated by local shock waves after bubble collapse.

Bubble growth and collapse were monitored in degassed test chambers (single bubble tests) as well as chambers that were not degassed (bulk cavitation). PSHPB testing in non-degassed chambers show initiation of bubbles and bulk cavitation with numerous bubbles. In this case, ‘spontaneous’ bubbles most likely nucleated or grew from microbubbles that were not initially visible but acted as natural seeds. Under similar test conditions, ‘spontaneous’ bubbles showed similar dynamic behavior to bubbles that were seeded, indicating that seeded single bubble cavitation tests capture relevant cavitation effects needed for investigating deformation and injury in tissues. However, maximum radii were smaller for the ‘spontaneous’ bubbles. Thus, lower collapse pressures are predicted for these bubbles.

In single bubble testing, maximum bubble size directly depended on the minimum underpressure, $P_{u\ min}$, applied which was in turn directly dependent on the applied PSHPB air gun pressure. Increasing magnitude of $P_{u\ min}$ resulted in larger bubble size. Secondary oscillatory bubble behavior was observed with coincident oscillations in the blast pressure profile. Bubble duration was short (–300 μs), and collapse was visually marked by fragmentation of the single bubble into clusters of multiple smaller bubbles. Calculated values for collapse pressure at the surface of the bubble also showed an

Table 2 Summary of cavitation and hydrogel slice test parameters

Group (size)	Edge placement ($n=6$)	Underneath placement ($n=7$)
Air gun pressure (kPa)	207	207
$P_{o\ max}$ (kPa)	1100 \pm 113	1088 \pm 86
$P_{u\ min}$ (kPa)	–207 \pm 32	–223 \pm 49
Lag time (μs)	61 \pm 7	53 \pm 6
Maximum R (mm)	2.35 \pm 0.34	2.54 \pm 0.63
P_c (kPa)	116.3 $\times 10^3$ \pm 8.8 $\times 10^3$	129.1 $\times 10^3$ \pm 12.2 $\times 10^3$
$P_c/P_{o\ max}$	–105.7	–118.7
Maximum* ε_{rr} with bubble expansion	–0.15 \pm 0.03	–0.23 \pm 0.06
Maximum ε_{rr} inertially-driven tension	0.12 \pm 0.02	–
Maximum* $\varepsilon_{\theta\theta}$ with bubble expansion	0.06 \pm 0.01	0.17 \pm 0.03
Maximum* ε_{VM} with bubble expansion	0.17 \pm 0.05	0.27 \pm 0.16
Maximum ε_{VM} after bubble collapse	–	0.35 \pm 0.16
Local shock area \dagger (mm^2)	–	0.18 \pm 0.03

* Maximum strain values in masked regions were not calculated

\dagger Based on strain threshold of $\varepsilon_{VM}>0.15$

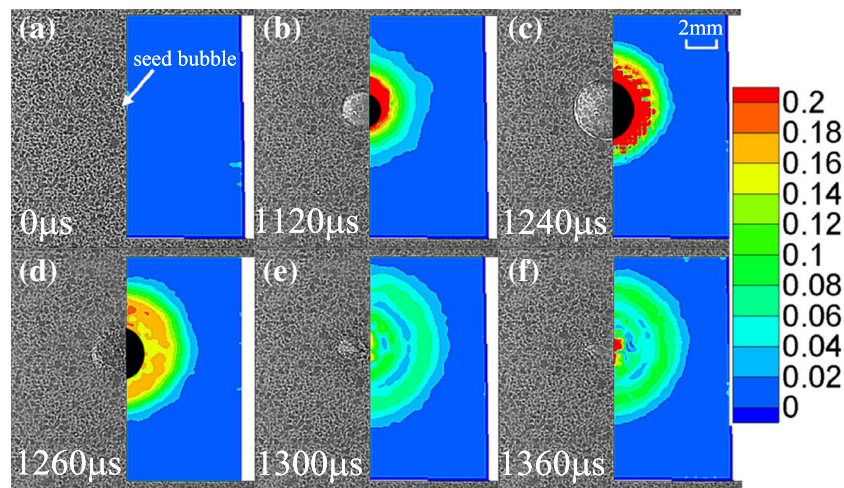


Fig. 9 Typical hydrogel deformation behavior for bubble cavitation underneath a speckled hydrogel slice. Left half of each of the high speed images show bubble growth (b and c) and collapse (d and e) at select time intervals and right half of each of the images show von Mises strain maps calculated using DIC. The dark region corresponds to the bubble overlap which causes distortion in the image and so no strains

were calculated in this region. Large compressive strains due to localized shock waves are measured at the bubble center after collapse (f). Strains greater than 0.2 were measured as listed in Table 2; the selected strain range highlighted patterns over the time range selected. $t=0$ corresponds to the start of the PSHPB experiment

approximately linear dependence with $P_{u\ min}$. Thus, underpressure determines the level of tissue-bubble interaction due to bubble growth and the effect of localized shock waves due to bubble collapse.

To appreciate the potential for cavitation to mediate blast injury, it is important to emphasize that even though the underpressure magnitude is significantly lower than the overpressure magnitude in the incident blast wave, the bubble collapse pressure is potentially much higher than the applied overpressure. This test system is uniquely suited to generate parametric conditions and test theoretical predictions about cavitation effects on tissue. For example, in Fig. 5(b) the predicted collapse pressures were up to the order of 100 times that of overpressure for tested conditions, and the test system was

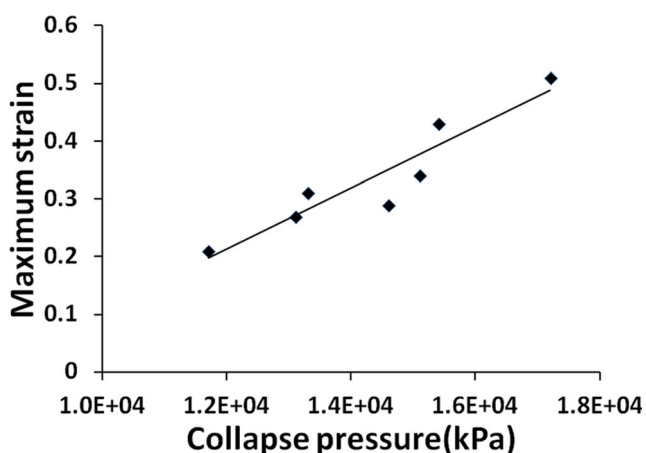


Fig. 10 Maximum von Mises strain, ε_{VM} , following bubble collapse is plotted against the calculated collapse pressure which drives the localized shock wave. Line corresponds to a linear fit ($R^2=0.87$)

able to capture material surface deformation and strain fields corresponding to local shock effects. These local shock waves emanate from the bubble site and decay rapidly over a short distance [11]. Corresponding tissue surrogate response was highly localized ($\sim 0.18\text{ mm}^2$) and of short duration ($<24\ \mu\text{s}$). Direct evidence of local shock waves was seen only when the tissue surrogate was in close proximity and when bubbles were placed underneath slices. Magnitude of these localized strains was found to be dependent on seed bubble distance and collapse pressure. Because of the novel nature of these experiments, comparative strain values for soft materials are lacking. Strain magnitude is also dependent on mechanical properties of the tissue surrogate. Localized strains were large (0.25 to 0.50) and predicted to be much larger than the compressive strains generated at earlier time points with passage of the simulated blast wave through the hydrogel. Large strains can contribute to localized damage. Such direct strain measures are useful since strain thresholds are often what have been reported for brain tissue injury [44–46]. Bain and Meaney [47] estimated *in vivo*, tissue-level, mechanical thresholds for axonal injury in the guinea pig optic nerve ranging from 0.13 to 0.34. Studies conducted by Morrison et al. [48, 49], also suggest that the brain cells are significantly damaged at strains >0.10 .

The test system can also be adapted to study tissue injury by replacing the hydrogel surrogate with cultured cells or tissue slices. Figure 11 shows the effect of cavitation events on a rat brain tissue slice during a simulated blast with bubble initiation and growth and collapse. Note that the maximum bubble size occurs at $t=1248\ \mu\text{s}$ where the tissue tearing starts to occur well after the bubble has collapsed at time $t=1704\ \mu\text{s}$ when localized tissue tearing was observed. These

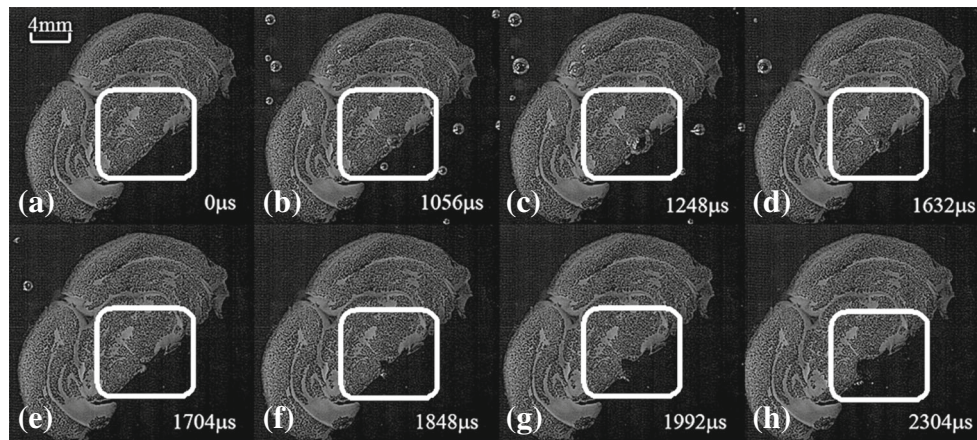


Fig. 11 Effect of cavitation on a rat brain tissue slice which was speckled and suspended in artificial cerebrospinal fluid. A simulated blast wave traveled from right to left with $P_{o\ max}=1045$ kPa and $P_{u\ min}=-203$ kPa. PSHPB testing showed bubble initiation (b), growth (b to d) and collapse (f). Cavitation-based damage with bubble collapse was observed in the

hypothalamus region (box). Tissue tearing was observed well after bubble collapse (f to h). Prior to testing, cell viability in 350 μm thick tissue slices was maintained by keeping them in artificial cerebrospinal fluid with 95 % O_2 and 5 % CO_2

observations reveal the potential for collapse events to deform and injure soft brain tissues.

Local deformations induced by direct bubble contact were also captured. Bubbles placed adjacent to the hydrogel slices rapidly expanded and then contracted, producing local deformations in the tissue surrogate. This resulted in compression of the hydrogel as well as tension due to dynamic rebounding of the impinging boundary. Maximum tensile strains were on the order of 80 % of the maximum compression strain. Comparing with the other test bubble configuration (underneath placement), these compressive and tensile strains are lower but over a longer time period. Such a dynamic response may be important when considering soft tissues which are more sensitive to damage in tension than compression. It is anticipated that in counter coup regions where cavitation was noted in previous *in vivo* impact studies [3, 50], tissue damage is more severe and this severity may be related to the either localized shock wave compression or the tensile component of the strain at the free boundaries of the brain where the tissue rebounds after the bubble collapse. The current experiments provide clear evidence predicting such damage to occur in brain tissue during improvised explosive device (IED) blasts.

Cavitation characterization relied on high speed imaging which was optimized to provide high resolution images at frame rates required to capture bubble dynamics. Pixel size resolution was limited when measuring initial seed bubble size and size of the collapsed bubble. Bubble overlap was also an issue in predicting maximum strains, since these regions were masked. DIC strain mapping also assumed 2D in-plane deformation; however, some out-of-plane effects were noted when bubbles were placed underneath the slice. As a result,

predicted strains were underestimated. Measured strains are also smaller than would be expected in brain tissues since the modulus of the hydrogels is slightly larger than for brain tissues [37].

Conclusions

A novel system was developed for cavitation testing and generating pressure pulses that mimicked a shock wave induced by an explosive blast, i.e., IED. Single bubble cavitation conditions were created and tested using a soft tissue surrogate. High speed bubble and hydrogel imaging data were used to elucidate cavitation effects including bubble impingement and secondary localized shock waves more powerful than blast overpressures. Both cavitation effects resulted in far greater strains than seen with initial passage of the overpressure component. Thus cavitation effects should be further investigated in tissues as a localized source of tissue injury. Future studies will further focus on testing effects of cavitation on brain tissue slices. Computational studies may also use deformation and strain maps to predict stresses within the tissue substrate.

Acknowledgments This research was funded by the Army Research Office award number W911NF-10-1-0276.

References

1. Elder GA, Cristian A (2009) Blast-related mild traumatic brain injury: mechanisms of injury and impact on clinical care. *Mt Sinai J Med* 76:111–118

2. Rosenfeld JV, McFarlane AC, Bragge P, Armonda RA, Grimes JB, Ling GS (2013) Blast-related traumatic brain injury. *Lancet Neurol* 12:882–893
3. Goeller J, Wardlaw A, Treichler D, O'Bruba J, Weiss G (2012) Investigation of cavitation as a possible damage mechanism in blast-induced traumatic brain injury. *J Neurotrauma* 29:1970–1981
4. Goldsmith W (2001) The state of head injury biomechanics: past, present, and future: part 1. *Crit Rev Biomed Eng* 29:441–600
5. Brennen CE (1995) Cavitation and bubble dynamics. Oxford University Press, New York
6. Harvey EN (1945) Decompression sickness and bubble formation in blood and tissues - harvey lecture, october 26, 1944. *Bull N Y Acad Med* 21:505–536
7. Apfel RE, Holland CK (1991) The likelihood of cavitation from short-pulse, low-duty cycle diagnostic ultrasound. *Ultrasound Med Biol* 17:179–185
8. Blatteau JE, Jean F, Pontier JM, Blanche E, Bompar JM, Meaudre E, Etienne JL (2006) Decompression sickness accident management in remote areas. Use of immediate in-water recompression therapy. Review and elaboration of a new protocol targeted for a mission at clipperton atoll. *Ann Fr Anest Reanim* 25:874–883
9. Gateau J, Taccoen N, Tanter M, Aubry JF (2013) Statistics of acoustically induced bubble-nucleation events in *in vitro* blood: a feasibility study. *Ultrasound Med Biol* 39:1812–1825
10. Shima A, Tsujino T, Hoyt JW, Taylor J (1981) A photographic study of cavitation in jet flow - discussion. *J Fluids Eng Trans ASME* 103:370–372
11. Vogel A, Lauterborn W, Timm R (1981) Optical and acoustic investigations of the dynamics of laser-produced cavitation bubbles near a solid boundary. *J Fluid Mech* 206:299–338
12. Jones IR, Edwards DH (1960) An experimental study of the forces generated by the collapse of transient cavities in water. *J Fluid Mech* 7:596–603
13. Tomita Y, Shima A (1986) A. Mechanisms of impulsive pressure generation and damage pit formation by bubble collapse. *J Fluid Mech* 169:535–564
14. Wang YC, Huang CH, Lee YC, Tsai HH (2006) Development of a pvdF sensor array for measurement of the impulsive pressure generated by cavitation bubble collapse. *Exp Fluids* 41:365–373
15. Benjamin TB and Ellis AT (1966) Collapse of cavitation bubbles and pressures thereby produced against solid boundaries. *Philos Trans R Soc Lond A Math Phys Sci* 260:221–228
16. Kornfeld M, Suvorov L (1944) On the destructive action of cavitation. *J Appl Phys* 15:495–506
17. Rayleigh (1917) On the pressure developed in a liquid during the collapse of a spherical cavity. *Philos Mag* 34:94–98
18. Plesset MS, Chapman RB (1971) Collapse of an initially spherical vapour cavity in neighbourhood of a solid boundary. *J Fluid Mech* 47:283–290
19. Moore DF, Jerusalem A, Nyein M, Noels L, Jaffee MS, Radovitzky RA (2009) Computational biology - modeling of primary blast effects on the central nervous system. *Neuroimage* 47:T10–T20
20. Nyein MK, Jason AM, Yu L, Pita CM, Joannopoulos JD, Moore DF, Radovitzky RA (2010) In silico investigation of intracranial blast mitigation with relevance to military traumatic brain injury. *Proc Natl Acad Sci U S A* 107:20703–20708
21. Shridharani JK, Wood GW, Panzer MB, Capehart BP, Nyein MK, Radovitzky RA, Bass CRD (2012) Porcine head response to blast. *Front Neurol* 3:70
22. Kenner VH, Goldsmit W (1973) Impact on a simple physical model of head. *J Biomech* 6:1–11
23. Lubock P, Goldsmith W (1980) Experimental cavitation studies in a model head-neck system. *J Biomech* 13:1041–1047
24. Gross AG (1958) A new theory on the dynamics of brain concussion and brain injury. *J Neurosurg* 15:548–561
25. Moss WC, King MJ, Blackman EG (2009) Skull flexure from blast waves: a mechanism for brain injury with implications for helmet design. *Phys Rev Lett* 103:2650–2665
26. Delius M (2002) Twenty years of shock wave research at the institute for surgical research. *Eur Surg Res* 34:30–36
27. Ohl CD, Arora M, Ikink R, de Jong N, Versluis M, Delius M, Lohse D (2006) Sonoporation from jetting cavitation bubbles. *Biophys J* 91:4285–4295
28. Okie S (2005) Traumatic brain injury in the war zone. *N Engl J Med* 352:2043–2047
29. Mayorga MA (1997) The pathology of primary blast overpressure injury. *Toxicology* 121:17–28
30. Harrison M (1952) An experimental study of single bubble cavitation noise. *J Acoust Soc Am* 24:454–454
31. Sarntinoranont M, Lee SJ, Hong Y, King MA, Subhash G, Kwon J, Moore DF (2012) High-strain-rate brain injury model using submerged acute rat brain tissue slices. *J Neurotrauma* 29:418–429
32. Ravichandran G, Subhash G (1994) Critical-appraisal of limiting strain rates for compression testing of ceramics in a split hopkinson pressure bar. *J Am Ceram Soc* 77:263–267
33. Subhash G, Ravichandran G (2000) Split Hopkinson pressure bar testing of ceramics. *Mech Test Eval ASM Int* 8:497–504
34. Subhash G, Liu Q, Moore DF, Ifju PG, Haile MA (2011) Concentration dependence of tensile behavior in agarose gel using digital image correlation. *Exp Mech* 51:255–262
35. Liu QL, Subhash G (2006) Characterization of viscoelastic properties of polymer bar using iterative deconvolution in the time domain. *Mech Mater* 38:1105–1117
36. Subhash G, Liu QL, Gao XL (2006) Quasistatic and high strain rate uniaxial compressive response of polymeric structural foams. *Int J Impact Eng* 32:1113–1126
37. Lee SJ, Sun J, Flint JJ, Guo S, Xie HK, King MA, Sarntinoranont M (2011) Optically based-indentation technique for acute rat brain tissue slices and thin biomaterials. *J Biomed Mater Res Part B* 97B:84–95
38. Van Dommelen JAW, Van der Sande TPJ, Hrapko M, Peters GWM (2010) Mechanical properties of brain tissue by indentation: Interregional variation. *J Mech Behav Biomed Mater* 3: 158–166
39. Pan B, Xie HM, Guo ZQ, Hua T (2007) Full-field strain measurement using a two-dimensional savitzky-golay digital differentiator in digital image correlation. *Opt Eng* 46:033601
40. Pan B, Qian KM, Xie HM, Asundi A (2009) Two-dimensional digital image correlation for in-plane displacement and strain measurement: a review. *Meas Sci Technol* 20:1–17
41. Nakase-Richardson R, McNamee S, Howe LL, Massengale J, Peterson M, Barnett SD, Harris O, McCarthy M, Tran J, Scott S, Cifu DX (2013) Descriptive characteristics and rehabilitation outcomes in active duty military personnel and veterans with disorders of consciousness with combat- and noncombat-related brain injury. *Arch Phys Med Rehabil* 94:1861–1869
42. Kato K, Fujimura M, Nakagawa A, Saito A, Ohki T, Takayama K, Tominaga T (2007) Pressure-dependent effect of shock waves on rat brain: Induction of neuronal apoptosis mediated by a caspase-dependent pathway. *J Neurosurg* 106:667–676
43. Long JB, Bentley TL, Wessner KA, Cerone C, Sweeney S, Bauman RA (2009) Blast overpressure in rats: recreating a battlefield injury in the laboratory. *J Neurotrauma* 26:827–840
44. Cullen DK, LaPlaca MC (2006) Neuronal response to high rate shear deformation depends on heterogeneity of the local strain field. *J Neurotrauma* 23:1304–1319
45. Cullen DK, Simon CM, LaPlaca MC (2007) Strain rate-dependent induction of reactive astrogliosis and cell death in three-dimensional neuronal-astrocytic co-cultures. *Brain Res* 1158:103–115

46. Geddes DM, Cargill RS, LaPlaca MC (2003) Mechanical stretch to neurons results in a strain rate and magnitude-dependent increase in plasma membrane permeability. *J Neurotrauma* 20:1039–1049
47. Bain AC, Meaney DF (2000) Tissue-level thresholds for axonal damage in an experimental model of central nervous system white matter injury. *J Biomech Eng Trans ASME* 122(6):615–622
48. Morrison B, Cater HL, Benham CD, Sundstrom LE (2006) An *in vitro* model of traumatic brain injury utilising two-dimensional stretch of organotypic hippocampal slice cultures. *J Neurosci Methods* 150(2):192–201
49. Morrison B, Meaney DF, Margulies SS, McIntosh TK (2000) Dynamic mechanical stretch of organotypic brain slice cultures induces differential genomic expression: relationship to mechanical parameters. *J Biomech Eng Trans ASME* 122(3):224–230
50. Kurosawa Y, Kato K, Saito S, Kubo M, Uzuka T, Fujii Y and Takahashi H (2009) Basic study of brain injury mechanism caused by cavitation. Conference proceedings: Annual International Conference of the IEEE Engineering in Medicine and Biology Society. *IEEE Eng Med Biol Soc Conf 2009*:7224–7227